A method to extrapolate the diffuse upwelling radiance attenuation coefficient to the surface as applied to the Marine Optical Buoy (MOBY)

Kenneth J. Voss, Physics Department, University of Miami, Coral Gables, FL. 33124.

Howard R. Gordon, Physics Department, University of Miami, Coral Gables, Fl. 33124.

Stephanie Flora, Moss Landing Marine Laboratory, San Jose State University, 95039.

B. Carol Johnson, Sensor Science Division, National Institute of Standards and Technology, Gaithersburg, MD 20877.

Mark Yarbrough, Moss Landing Marine Laboratory, San Jose State University, 95039.

Michael Feinholz, Moss Landing Marine Laboratory, San Jose State University, 95039.

Terrence Houlihan, Moss Landing Marine Laboratory, San Jose State University, 95039.

Corresponding author: Kenneth Voss, Physics Department, University of Miami, Coral Gables, FL 33124, voss@physics.miami.edu

Abstract: 250 words

The upwelling radiance attenuation coefficient (K_{Lu}) in the upper 10 m of the water column can be significantly influenced by inelastic scattering processes, and thus will vary even with homogeneous water properties. The Marine Optical BuoY (MOBY), the primary vicarious calibration site for many ocean color sensors, makes measurements of the upwelling radiance (L_u) at 1 m, 5 m, and 9 m and uses these values to determine K_{Lu} and propagate the upwelling radiance directed toward the zenith, L_u, at 1 m to and through the surface. Inelastic scattering causes the K_{Lu} derived from the arm measurements to be an underestimate of the true K_{Lu} from 1 m to the surface at wavelengths greater than 570 nm, thus the derived water leaving radiance is underestimated at wavelengths longer than 570 nm. A method to correct this K_{Lu} , based on a model of the upwelling radiance including Raman scattering and chlorophyll fluorescence has been developed which corrects this bias. The model has been experimentally validated, and this technique can be applied to the MOBY data set to provide new, more accurate products at these wavelengths. When applied to a 4 month MOBY deployment, the corrected water leaving radiance, L_w, can increase by 5% (600 nm), 10% (650 nm) and 50% (700 nm). This method will be used to provide additional more accurate products in the MOBY data set.

1. Introduction

The Marine Optical Buoy (MOBY) (Clark *et al.* 1997, 2002) has been the primary vicarious calibration site for many, if not all, ocean color satellite instruments since 1997 (Barnes et al. 2001, Eplee et al. 2001, Franz et al. 2007, Wang et al. 2013). This data set provides the water leaving spectral radiance, $L_w(\lambda)$, and normalized water leaving radiance, $L_{wn}(\lambda)$, to satellite programs for use in the vicarious calibration process (Clark *et al.*, 1997), and as such is required to provide these parameters with the highest possible accuracy. MOBY has three arms, at 1 m, 5 m, and 9 m depth, for measuring the upwelling radiance, $L_u(\lambda, z)$, so the shallowest depth that MOBY measures L_u is at 1 m. To propagate this measurement to the surface requires an estimate of $K_{Lu}(\lambda, 0, 1)$, the diffuse upwelling radiance attenuation coefficient for the depths from 0 m – 1 m (hereafter referred to as K01 for simplicity). The diffuse attenuation coefficient between depths z_1 and z_2 is defined as

$$K_{Lu}(\lambda, z_1, z_2) = -\frac{\ln[L_u(\lambda, z_2) / L_u(\lambda, z_1)]}{z_2 - z_1}.$$

Also needed are the transmission of the air-sea interface for upwelling radiance, and the index of refraction of the water to account for refractive effects on the radiance due to the air-sea interface. These latter two parameters are assumed to be constant but K01 is variable and must be determined for each data set.

The current estimate of K01 is derived by using this upper arm measurement at 1 m, combined with either the measurement of $L_u(\lambda, z)$ at 5 m or 9 m. In general, the pair of measurements at 1 m and 5 m are used to form $K_{Lu}(\lambda, 1, 5\text{ m})$ (K15) and this is assumed to represent K01. For the MOBY products named L_w1, and $L_{wn}1$, $L_u(\lambda, 1\text{m})$ is propagated to the surface using K15. For wavelengths greater than 570 nm, in the clear water where MOBY is located, because of inelastic processes, both due to Raman scattering (Sugihara et al. 1984) and due to chlorophyll fluorescence (Gordon 1979), $K_{\mathrm{Lu}}(\lambda)$ is not constant with depth. In general, for these wavelengths K15 will be less than K01 due to the increasing fraction of light that has been inelastically scattered from the blue region of the spectrum, where energy is abundant, to the red region, where the incoming light is rapidly attenuated. It has been pointed out that using K15 in place of K01 in the region above 570 nm causes the $L_{\mathrm{w}}(\lambda)$ and $L_{\mathrm{wn}}(\lambda)$ derived from MOBY to be an underestimate of their true values. (Li et al., 2016). This paper will describe a method to estimate the correct K01 using a validated model of K01 in terms of K15 and K19 along with the measured K15 and K19

2. Model and validation

As described above, the goal is to develop a model for estimating K01 given K15, K19, or K59 or some combination of these. The model is derived by simulating the in-water light field utilizing radiative transfer computations.

The site where MOBY is located, off of the island of Lanai, Hawaii, can typically be considered Case 1 waters, meaning that the inherent optical properties (absorption and scattering coefficients, etc.) covary with the concentration of Chlorophyll a (Chl) (Morel and Prieur 1977), and can be modeled using the single parameter Chl. At the site, the range of Chl is also quite limited and is between 0.05 mg/m^3 and 0.15 mg/m^3 over 98% of the time. In addition, since the MOBY measurements are made for the specific purpose of satellite vicarious calibration, the measurements are usually performed within 3 h of solar noon, which results in a somewhat limited range of solar zenith angles (<50°). Thus the parameter space which must be filled with model results is limited. With these constraints, a Monte-Carlo radiative transfer model, including Raman inelastic scattering was used to determine K01, K15 and K19 for four values of Chl (0 mg/m^3, 0.05 mg/m^3, 0.10 mg/m^3, 0.15 mg/m^3), six solar zenith angles (SZA=10°, 20°, 30°, 40°, 50°, and 60°), and for every 10 nm from 400 to 700 nm.

As expected, the results from this Monte Carlo model show that K_{Lu} depends on the pair of depths used, Chl, and solar zenith angle. Figure 1 shows the Monte Carlo results for 3 different Chl values for K01 as a function of wavelength at 10° SZA. Also shown are K15/ K01, K59/ K01, and K19/ K01 for the 3 Chl values. For wavelengths less than 575 nm, K01 is the same as K15 and K19 to within 3%. Above 575 nm, the K_{Lu}'s rapidly diverge. The effect of using one of these K_{Lu} values to provide K01 would be to underestimate L_w or L_{wn} in this spectral region. Above 700 nm the values would continue to diverge, but because of issues such as instrument self-shadowing (Gordon and Ding, 1992; Mueller, 2007) and very small L_w, MOBY data above 700 nm are not used for vicarious calibration, and will not be discussed in this paper.

Other features to note in Fig. 1 are that the best approximation for K01 is K15 followed by K19. K59 deviates the most from K01. When an error analysis is carried out on the various environmental effects that can interfere with the calculation of $K_{Lu}(\lambda)$, excluding inelastic effects, K19, because it spans a larger depth range, has the least uncertainty. Thus, we will concentrate on the relationship between K15 (because it is the closest to K01) and K19 (because it theoretically should have the least uncertainty), and not discuss K59 until the appendix.

$K_{Lu}(\lambda)$ also depends on the solar zenith angle. Figure 2 shows the variation of the modeled K01 with SZA, Chl is 0.10 mg/m^3. As expected, particularly for wavelengths above 600 nm, there is a stronger dependence on solar zenith angle at angles greater than 30° than on Chl, for the range of Chl expected at the MOBY site. Fortunately, for any specific measurement the solar zenith angle is known, so an appropriate set of K_{Lu}'s can easily be determined.

To validate these model results, we used a dataset of hyperspectral $L_u(\lambda,z)$ measurements performed in the Hawaiian islands (Yarbrough *et al*., 2007a). It is difficult to make measurements both near the surface, and in the region above 600 nm, where instrument self-shading is a large factor due to the high absorption of water itself. A specialized instrument was developed to operate in this spectral region, which was based on a Remotely Operated Vehicle (ROV) with a fiber collector extending a meter in front of the ROV. (Yarbrough et al. 2007b). The fiber extended from the ROV to the ship, where it was coupled to a spectrometer with 1 nm resolution from 350 nm to 900 nm. The ROV was placed at several different depths, so profiles of the near surface water column could be obtained. A subset of data from this experiment was selected to validate these model results. We selected profiles that were in deep water, had measurement depths within 10 cm of the surface paired with measurements at least 1 m and 5 m depths (but often there was also a measurement at 9 m depth), and were performed in a reasonably short period of time. As part of the criteria, the K_{Lu}'s derived from the measurement pairs had to agree to within 0.03 m^{-1} for the wavelength range from 400 nm to 550 nm.

Figure 3 shows the comparison between the model and ROV data for 4 representative data sets. The model results here assume a Chl value of 0.10 mg/m^3 and the model results are interpolated to match the SZA of the data. It shows that the model represents the measured K15 and K01 reasonably well except for the region between 660 and 700 nm where chlorophyll fluorescence (which was not included in the original model) is important. Making a model which includes this fluorescence from first principles is difficult because, as opposed to Raman which depends on the physical properties of water (Bartlett et al., 1998), chlorophyll fluorescence depends not only on the amount of chlorophyll in the water, but also on the physiological status of the phytoplankton containing the chlorophyll (Keifer, 1973). The light history, packaging, and many other factors can affect the quantum efficiency of fluorescence, η, and thus, the depth of the feature, or "Dip", in K_{Lu}. To include the Dip in our model requires that we use more information from each individual data set.

To determine the magnitude of the Dip in K_{Lu} we went back to our ROV data set and relaxed the selection criteria to include more data. In this case we allowed measurements that varied less than 0.1 m^{-1} in the region between 400 and 550 nm, and additionally required that $K_{Lu} < 1$ m^{-1} between 660 and 700 nm. This had the effect of excluding data that had larger variations of surface irradiance during measurement than we could handle with the typical downwelling sky irradiance, *Es*, normalization procedures. We then formed a baseline using measurements at

660 nm and 700 nm, and found the difference between this baseline and the measured K_{Lu} for each K_{Lu} (K01, K15, K19, and K59). Each data set was then normalized to the value at 681 nm, to derive an overall shape for the Dip. The average shape and standard deviation is shown in Fig. 4. The sharp feature in the data at 687 nm is caused by an atmospheric oxygen absorption band at this wavelength, and the associated line filling, similar to Fraunhofer line filling (Ge *et al.*, 1995). This is illustrated by including results of modeling this chlorophyll Dip with and without the oxygen feature, as shown in Fig. 4. In this figure the model assumed Chl = 0.1 mg/m^3, SZA= 10°, and η=0.045. What can be seen, however, is that the average of the data is a very good representation of the Dip (the standard deviation is small) and we use this average to develop our correction to K01 for this feature.

To handle the variation of the Dip with the physiological parameters of the phytoplankton, we investigated the data and found there was a consistent relationship between the depth of the Dip at 681 nm in K15 (Dip15) and K19 (Dip19) as shown in Fig. 5. We also found that while there was a relationship between Dip15 and Dip19 (r^2 =0.69), there was not a relationship between either Dip15 and Dip01 (r^2=0.003) or between Dip19 and Dip01 (r^2=0.019). There was also not a relationship between Dip05 and Dip59. There was also no dependence of Dip01 with Chl or incident irradiance (although all the data, as with MOBY data, were collected within ±2 h of solar noon). Thus we were forced to assume a constant value of -0.10 m^{-1} ± 0.02 m^{-1} for the Dip01 at 681 nm.

3. Correction algorithm

We now have validated all of the steps necessary to form a correction algorithm for the inelastic effects. The steps in the correction algorithm for each data set are:

1) Interpolate the model K_{Lu} tables to get the correct model K_{Lu}'s for the specific solar zenith angle of that data set. The model was also interpolated to the MOBY wavelengths using a spline interpolation.

2) Use the solar zenith interpolated tables to find which Chl (used as an index) forms the best match between measured and modeled K15 and K19 at 500 nm. Using the average of these two retrieved values for Chl, interpolate the tables to find K01.

3) Add the average Dip01 scaled by -0.10 m^{-1} at 681 nm.

4) Below 500 nm $K01_{final}$ is the average of the measured values K15 and K19.

5) Above 570 nm, $K01_{final}$ is the modeled K01.

6) Because the measured K15 and K19 is a very good representation of K01 in the region below 570 nm, see Fig. 1, the modeled K01 is blended into the average of the measured K15 and K19 over the region from 500 to 570 nm using the equation:

$$\mathrm{K01}_{\mathrm{final}}(\lambda) = \frac{(\lambda - 500\mathrm{nm})}{70\mathrm{nm}}\mathrm{K01} + \frac{(570\mathrm{nm} - \lambda)}{70\mathrm{nm}}(\mathrm{K15} + K19)/2 \tag{3}$$

This $K01_{final}$ can then be used in the data reduction process to propagate $L_u(\lambda, 1$ m) to the surface to find $L_w(\lambda)$ and $L_{wn}(\lambda)$. Along with this, we can get an estimate of the uncertainty in this value if we look at the differences between the correction predicted from the two measured K_{Lu}'s. Note that this uncertainty only reflects the uncertainty introduced by this process, and not the uncertainty in the fundamental values of K15 and K19. For the region below 500 nm, the uncertainty in the K_{Lu} correction can be obtained by the difference in the measured K15 and K19. Following section 4.3.6 of the GUM 2008 (JGCM, 2008) we estimate the uncertainty below 500 nm to be:

$$\frac{|K15 - K19|}{2} \tag{4}$$

Above 570 nm this uncertainty is given by:

$$\frac{|K01(K15) - K01(K19)|}{2} \tag{5}$$

where K01(K15) refers to the K01 derived from the Chl found in the K15 measurement, and K01(K19) refers to the K01 derived from the Chl found in the K19 measurement. The region between 500 nm and 570 nm blends these two values, as in Eq. 3.

To show the effect this has on a set of MOBY data, Fig. 6 shows the original K_{Lu} used to propagate the $L_u(\lambda, 1\ \ \mathrm{m})$ to the surface, along with the new modeled $K01_{final}$. In addition, it shows the results of the uncertainty calculation as described above. For most of the spectra, as expected, $K01_{final}$ has not changed. However, above 550 nm it starts to depart and rapidly becomes much larger than the original K_{Lu}. The uncertainty meanwhile is much less than 0.01 m^{-1} through much of the spectrum, but increases in the red to be on the order of 0.01 m^{-1} to 0.02 m^{-1}, much smaller than the difference between the original and modeled K_{Lu}.

Figure 7 shows the effect of this change on the calculated L_w, which we call L_w*21* to differentiate it from the heritage L_w*1*. The major effect is in the red wavelengths, where L_w is very small in either case. As can be seen in the right panel of Fig. 7, while there is no change below 550 nm, the percent difference between the old and new L_w grows to be on the order of 50% by 700 nm. For the region between 600 nm and 700 nm, this correction makes a significant difference to the data.

Figures 8 and 9 show the effect of using $K01_{final}$ in the calculation of L_w when averaged over several bands of the Sentinel 3A Ocean Land Color Instrument (OLCI) (Donlon *et al*. 2012). In Fig. 8, there is little to no effect in the blue and green wavelengths as would be expected. However, Fig. 9 shows that there is a significant difference for the channels between 600 nm and 700 nm. This change is much larger than our uncertainty of the correction, and shows that this correction reduces a significant bias in the MOBY data set at these wavelengths.

4. Conclusion

We have shown that there is a significant bias in the MOBY L_w and L_{wn} data set for wavelengths above 570 nm due to the influence of Raman scattering and Chl fluorescence in the estimation of K_{Lu}. With a validated model, we can use the existing measurements of K15 and K19 to adjust the model for K01 for each data set. We can also use this to estimate the uncertainty in the K01 used to propagate $L_u(\lambda,1\text{ m})$ to the surface to produce L_w (L_w21) and L_{wn} ($L_{wn}21$) for satellite vicarious calibration.

While we have concentrated this work on illustrating the effect and developing a correction algorithm specifically for the MOBY sensor, this work may be generalized in that all in-water measurements must account for this non-linear K_{Lu} near the surface for wavelengths greater than approximately 550 nm. This is applicable both to systems that have fixed measurement depths and profiling systems. It is obvious from this work, that for fixed measurement depth systems, such as MOBY, a correction, using models must be made. Note that for a similar system, the BOUSSOLE site, the modeled Lw includes the effect or Raman, but not Chl flouresence. (Antoine et al., 2008) However, it is also true that for profiling systems the effect of Raman scattering must be taken into account. Seldom, in real world situations, can accurate measurements of the upwelling radiance be made in upper 1 m of the water column. It is often the case that, to reduce noise, the measurements in the upper 10 m of the water column of a profile are accumulated to extrapolate the measurements to the upwelling radiance just below the surface (Zibordi *et al*., 2011). Often this extrapolation is done assuming a logarithmic decay of the radiance with depth, which is similar to assuming that the K_{Lu} is constant with depth. As has been shown, this is not the case at these longer wavelengths and either modeling must be done to extrapolate the measurements to the surface, or, at the least, the extrapolation must be done allowing for a non-linear decay of the log transformed radiance with depth.

Acknowledgements

This work was supported by NOAA under grant NA15OAR4320064 and by NASA under grant NNX14AP63G and grant NNH11AQ89I.

Appendix A

The preferred MOBY data product for vicarious calibration of ocean color satellites is the L_w1 or $L_{wn}1$ product. As discussed earlier, this product uses $L_u(\lambda, 1m)$ and K15 to generate $L_u(\lambda, 0\text{-})$, the upwelling radiance just below the sea surface, which is then transmitted through the surface to form L_w1 or $L_{wn}1$, the latter after normalization by the downwelling surface irradiance.

While MOBY has arms, and measurements, at 1 m, 5 m, and 9 m, at times the measurements from one of the arms is not available, limiting the options for deriving $L_u(\lambda, z)$ or K_{Lu}. When the 5 m arm is unavailable, we must use K19 to propagate $L_u(\lambda, 1m)$ to the surface and this product is named L_w2 (or $L_{wn}2$). In this case the technique described in the text can be used, but the estimation of K01 must depend only on K19, and will be called L_w22 (or $L_{wn}22$) to differentiate it from L_w21. This does not have a large effect on the processing, as in general the K01 predicted from K15 and K19 agree quite well. Unfortunately, it is more often the case that if an arm is not available, it is the upper arm that is missing. In this case one is left with K59 and propagating $L_u(\lambda, 5m)$ to the surface to form $L_u(\lambda, 0\text{-})$, this product is called L_w7 and $L_{wn}7$. As was shown in Fig. 1, K59 is affected much more strongly than K15 or K19 by inelastic processes, and the propagation to the surface of $L_u(\lambda, 5m)$ is very sensitive to the K_{Lu} used. In addition, we are not modeling K01, but rather K05. However, we can still generate an algorithm that can improve our L_w7 and $L_{wn}7$ product.

In this variation of the algorithm we use K59 to generate a model K05, in a manner similar to the method described earlier. The Dip05, derived from an average of experimental data, as before, has a magnitude of 0.085 $m^{-1} \pm 0.009$ m^{-1} at 681 nm.

To generate the uncertainty for this new product (called $L_{w}27$ or $L_{wn}27$) we can look at how well $L_{w}27$ agrees with these other products when we have all 3 arms available. A similar situation occurs if we are missing either the 5 m or 9 m measurement, the uncertainties have to be based on how well the final products statistically agree with each other when all three arms are available. Figure 10a shows a comparison between 4 products, $L_{w}1$, $L_{w}7$, $L_{w}21$, and $L_{w}27$ for Band 8 (665 nm) on the Sentinel 3 OLCI sensor. These products were generated for a recent MOBY deployment (M253) for which all arms were operational. The OLCI sensor is chosen as an example because it has several bands in the wavelength range between 600 and 700 nm. As can be seen, the heritage products $L_{w}1$ and $L_{w}7$ are significantly different than $L_{w}21$ and $L_{w}27$, however the $L_{w}21$ and $L_{w}27$ agree with each other quite closely. To see this agreement more quantitatively, Fig. 10b shows a histogram of the percent difference between $L_{w}21$ and $L_{w}27$. There is only a -1.2% bias (with a standard deviation of 7%) between these two products. This can be compared to the 20% bias between $L_{w}21$ and $L_{w}1$, and 186% bias between $L_{w}27$ and $L_{w}7$. $L_{w}27$ is a significant improvement over $L_{w}7$, and a good substitute for $L_{w}21$ when the top arm is unavailable.

References

Antoine, D., F. d'Ortenzio, S. B. Hooker, G. Becu, B. Gentili, D. Tailliez, and A. J. Scott, 2008: Assessment of uncertainty in the ocean reflectance determined by three satellite ocean color sensors (MERIS, SeaWiFS and MODIS-A) at an offshore site in the Mediterranean Sea (BOUSSOLE project). J. Geophys. Res., 113, C07013, 10.1029/2007JC004472.

Barnes, R.A., R.E. Eplee, Jr., G.M. Schmidt, F.S. Patt, and C.R. McClain, 2001: The calibration of SeaWiFS, Part1: Direct techniques. *Appl Opt*., **40**, 6682-6700, 10.1364/AO.40.006682.

Bartlett, J. S., K.J. Voss, S. Sathyendranath, and A. Vodacek, 1998: Raman scattering by pure water and seawater. *Appl*. *Opt*., **37**, 3324 – 3332, doi: 10.1364/AO.37.003324.

Clark, D.K, H.R. Gordon, K.J. Voss, Y. Ge, W. Broenkow and C.C. Trees, 1997: Validation of atmospheric corrections over oceans. *J. Geophs. Res*., **102,**17209-17217, doi: 10.1029/96JD03345.

Clark, D.K, M.A. Yarbrough, M.E. Feinholz, S. Flora, W. Broenkow, Y.S. Kim, B.C. Johnson, S.W. Brown, M. Yuen and J.L. Mueller, 2002: MOBY, a radiometric buoy for performance monitoring and vicarious calibration of satellite ocean color sensors: Measurement and data analysis protocols. *Ocean Optics Protocols for Satellite Ocean Color Sensor Validation, Revision 3, Volume 2*. J.L. Mueller and G.S. Fargion, Eds. Greenbelt, MD, NASA Goddard Space Flight Center. **NASA/TM--2002-21004,** 138-170.

Donlon, C., B. Berruti, A. Buongiorno, M.-H. Ferreira, P. Féménias, J. Frerick, P. Goryl, U. Klein, H. Laur, C. Mavrocordatos, J. Nieke, H. Rebhan, B. Seitz, J. Stroede, R. Sciarra, 2012: The Global Monitoring for Environment and

Security (GMES) Sentinel-3 mission. *Remote Sensing of the Env.*, 120, 37-57, doi:10.1016/j.rse.2011.07.024.

Eplee, R.E., Jr., W.D. Robinson, S.W. Bailey, D.K. Clark, P.J. Werdell, M. Wang, R.A. Barnes, and C.R. McClain, 2001: The calibration of SeaWiFS, part 2: Vicarious techniques. *Appl. Opt.*, **40**, 6701-6718, doi: 10.1364/AO.40.006701.

Franz, B.A., S.W. Bailey, P.J. Werdell, and C.R. McClain, 2007: Sensor-independent approach to the vicarious calibration of satellite ocean color radiometry. *Appl. Opt.* **46**, 5068-5082, doi: 10.1364/AO.46.005068.

Ge,Y., K.J. Voss, and H.R. Gordon, 1995. In situ measurements of inelastic scattering in Monterey Bay using solar Fraunhofer lines. *J. Geophys. Res.*, **100**, 13,227 - 13,236, doi: 10.1029/95JC00460.

Gordon, H.R.,1979: Diffuse reflectance of the ocean: the theory of its augmentation by Chlorophyll a fluorescence at 685 nm. *Appl. Opt.*, **18**, 1161-1166, doi: 10.1364/AO.18.001161.

Gordon H.R., Ding K., 1992: Self-shading of in-water optical instruments. *Limnol. Oceanogr.,* **37**, 491–500, doi: 10.4319/lo.1992.37.3.0491.

JCGM, 2008: Evaluation of measurement data – Guide to the expression of uncertainty in measurement. Joint Committee for Guides in Metrology, *http://www.bipm.org/utils/common/documents/jcgm/JCGM_100_2008_E.pdf*.

Kiefer , D.A., 1973: Fluorescence properties of natural phytoplankton populations. *Marine Biology*, **22**, 263-269, doi: 10.1007/BF00389180.

Li L., D. Stramski, and R.A. Reynolds, 2016: Effects of inelastic radiative processes on the determination of water-leaving spectral radiance from extrapolation of underwater near-surface measurements, *Appl. Optics*, 55, 7050-7067, doi: 10.1364/AO.55.007050.

Morel, A., and L. Prieur, 1977: Analysis of variations in ocean color. *Limnol. Oceanogr.*, **22**, 709-722, doi: 10.4319/lo.1977.22.4.0709.

Mueller, J., 2007: Self-shading corrections for MOBY upwelling radiance measurements. Final Rep., NOAA Grant NA04NESS4400007, 33 pp. [Available online at http://moby.mlml.calstate.edu/sites/default/files/2007_NOAA_Self-Shading Corrections for MOBY.pdf.]

Sugihara, S., M. Kishino, and M. Okami,, 1984: Contribution of Raman scattering to upward irradiance in the sea. *J. Oceanogr. Soc. Japan*, **40**, 397-404, doi: 10.1007/BF02303065.

Wang, M., X. Liu, L. Tan, L. Jiang, S.H. Son, W. Shi, K. Rausch, and K. Voss, 2013: Impacts of VIIRS SDR performance on ocean color products. *J. Geophys. Res.: Atmosph*. **118**, 1-14, doi:10.1002/jgrd.50793.

Yarbrough, M.A., M.E. Feinholz, S. Flora, T. Houlihan, B.C. Johnson, Y.S. Kim, M.Y. Murphy, M. Ondrusek, and D.K. Clark, 2007a: Results in coastal waters with high-resolution *in-situ* spectral radiometry: The Marine Optical System ROV. *Proc. SPIE 6680, Coastal Ocean Remote Sensing*. 66800I, doi:10.1117/12.735064.

Yarbrough, M.A., S. Flora, M.E. Feinholz, T. Houlihan, Y.S. Kim, S.W. Brown, B.C. Johnson, K. Voss, and D.K. Clark, 2007b: Simultaneous measurement of up-welling spectral radiance using a fiber-coupled CCD spectrograph. *Proc. SPIE 6680, Coastal Ocean Remote Sensing*, 66800J: doi: 10.1117/12.735016.

Zibordi, G., Berthon, J.-F., Mélin, F., and D'Alimonte, D.,2011: Cross-site consistent in situ measurements for satellite ocean color applications: The BiOMaP radiometric dataset, *Remote Sensing of Environment* **115**, 2104-2115.

Figure Captions

Figures

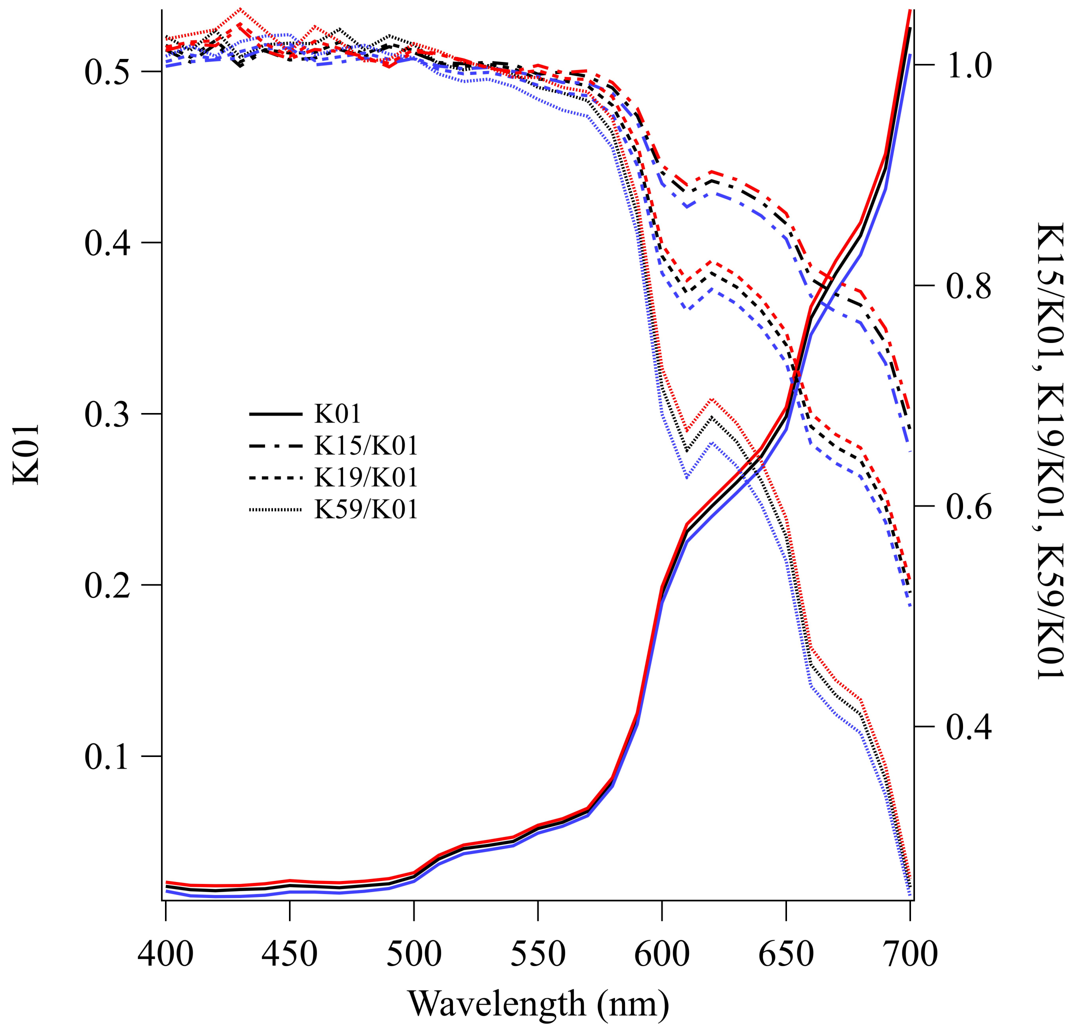

Figure 1) Modeled K01 (left axis) along with the modeled ratios K15/ K01 and K19/ K01 and K59/ K01 (right axis) for Chl = 0.05 mg/m^3 (blue), Chl = 0.10 mg/m^3 (black), and Chl = 0.15 mg/m^3 (red), all at 10° SZA.

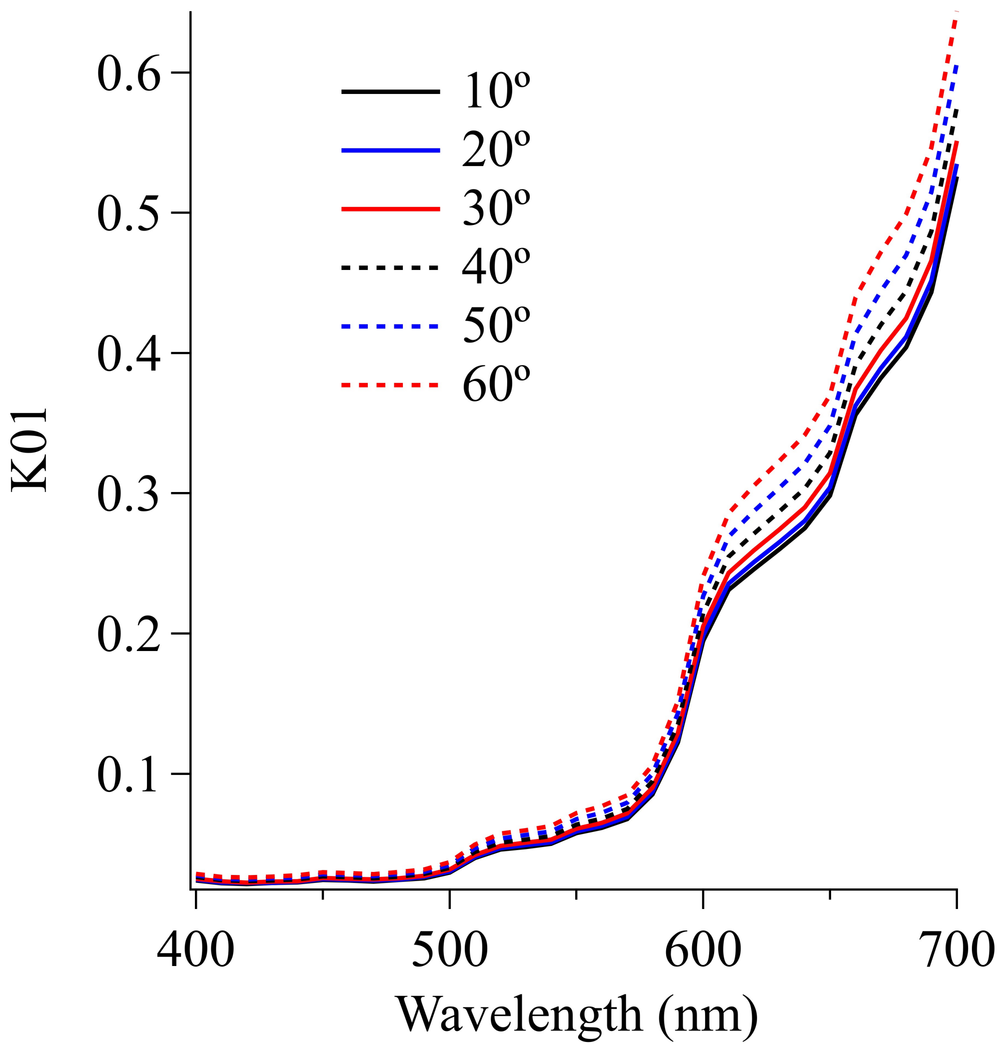

Figure 2) Variation in modeled K01 with wavelength and solar zenith angle, with Chl= 0.1 mg/m^3.

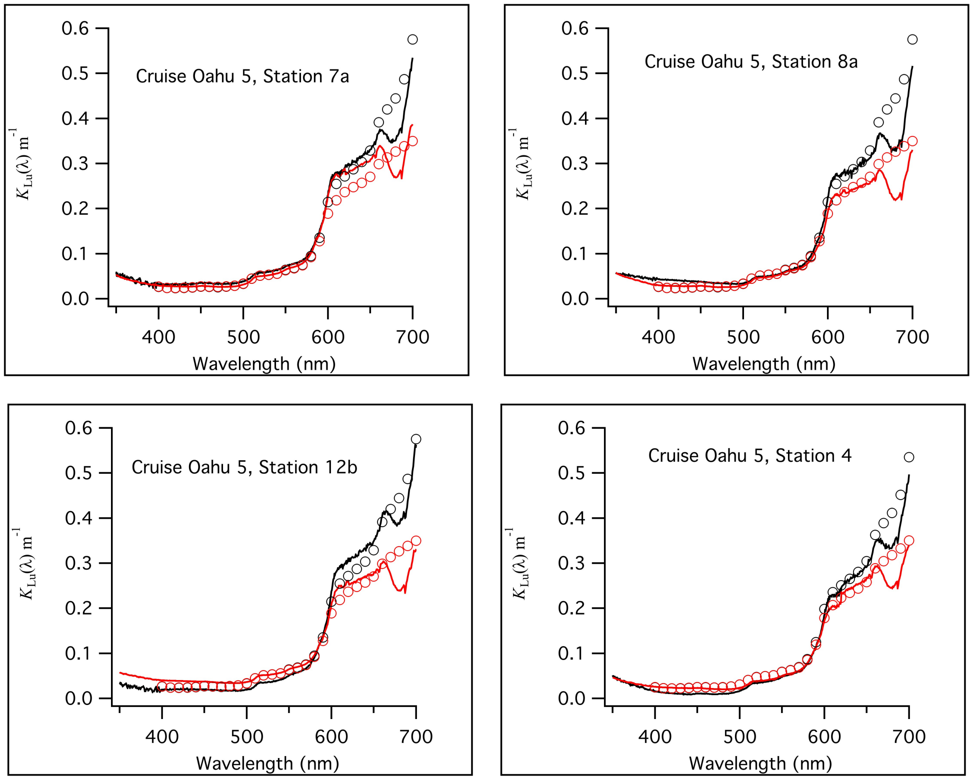

Figure 3) Comparison of modeled and ROV data. The model is displayed as circles, data as solid lines. Red represents K15 while black is K01. Model data were interpolated to appropriate solar zenith angle, but assumed a constant Chl value of 0.10 mg/m^3. Note in these graphs, the effect of Chl fluorescence has not been included in the model results.

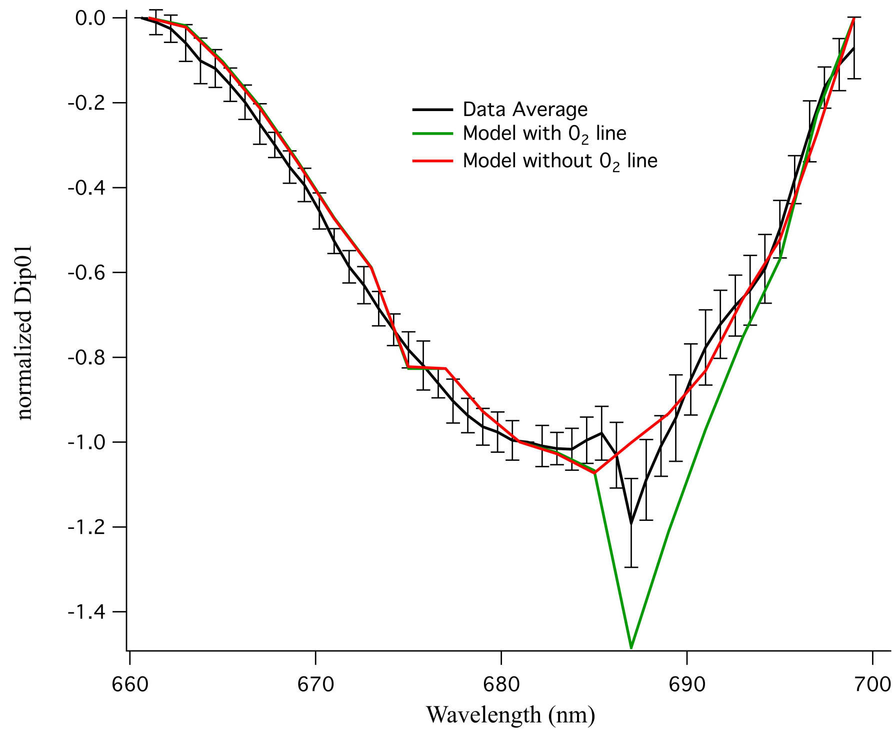

Figure 4) The deviation of K_{Lu} from a straight baseline between 660 nm and 700 nm, due to Chl fluorescence and an atmospheric oxygen absorption band at 687 nm. The average of the data is shown, along with the standard deviation of this average. Also shown are the model results with and without the oxygen band. In the model the Chl = 0.1 mg/m^3, SZA= 10°, and η=0.45.

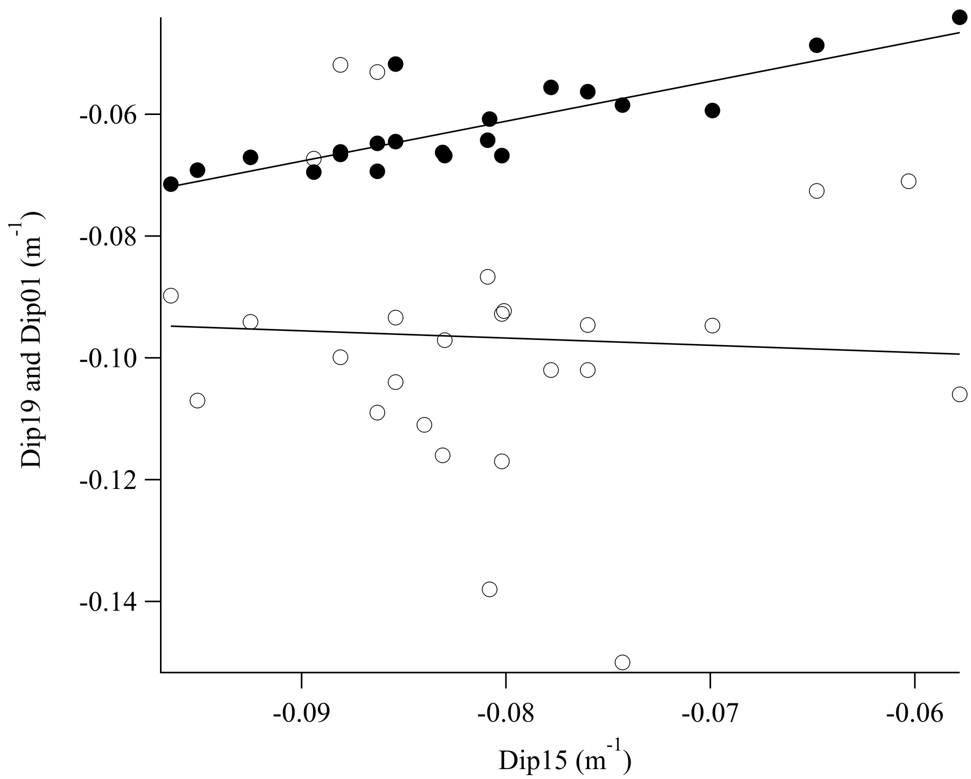

Figure 5) Dip19 and Dip01 versus Dip15 (all values for the Dip at 681 nm). The lines are a linear least square fit to the data. Dip19 are filled circles while Dip01 are open circles. As can be seen Dip15 and Dip19 have a relationship with each other (r^2=0.69) while Dip01 and Dip15 have no significant relationship (r^2=0.003).

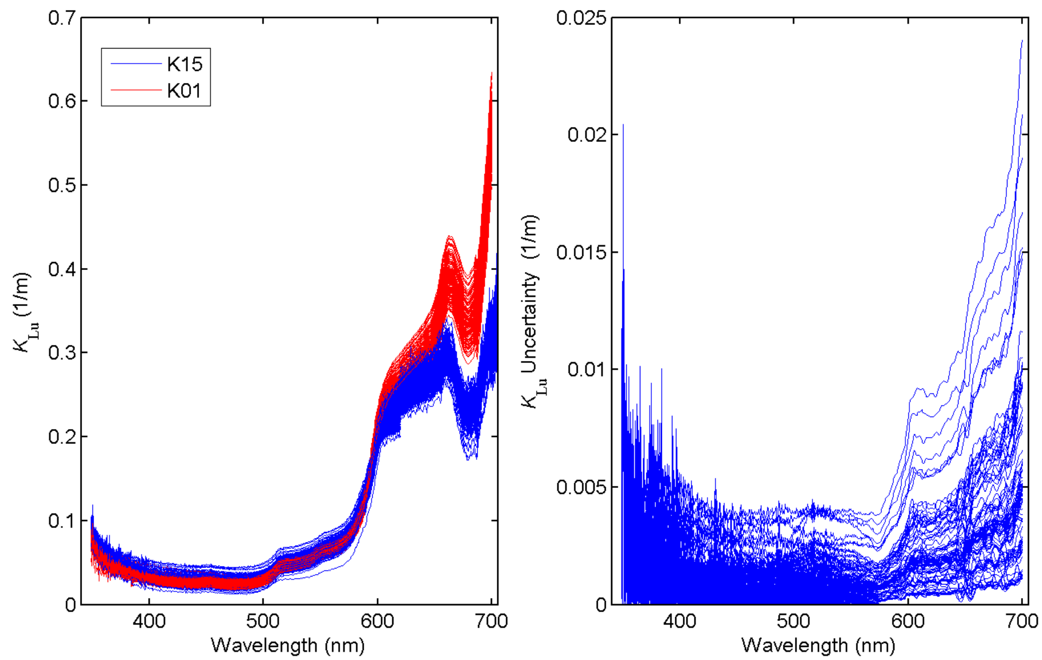

Figure 6) The modeled $K01_{final}$ along with the original K15 for a full MOBY deployment (M253). The left panel shows the K_{Lu} values, while the right panel shows our estimated uncertainty associated with the correction procedure.

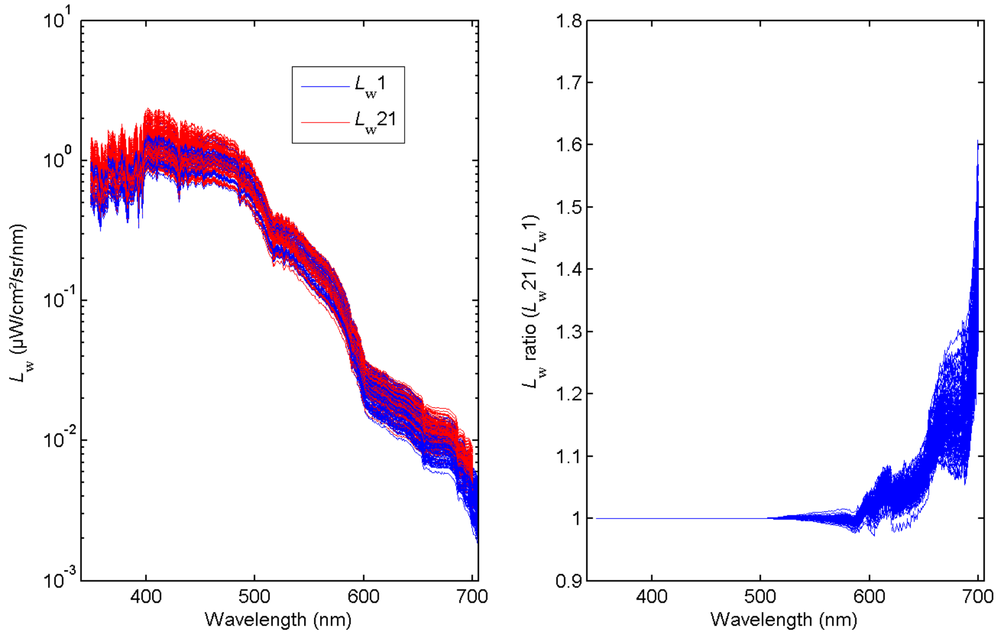

Figure 7) Effect of using K01$_{final}$ rather than K15 on the retrieved L_w. The left panel shows the L_w1 and L_w21, while the right panel shows L_w21/ L_w1. There is no effect before 550 nm, above which the difference grows to 50%.

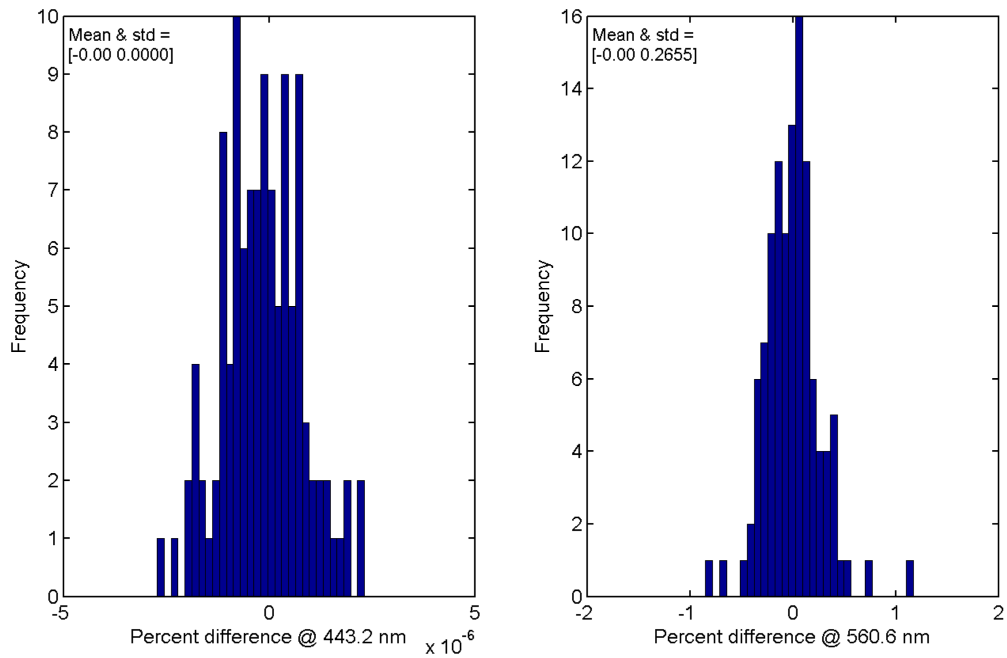

Figure 8) Histograms of the 100*(L_w21 - L_w1)/ L_w21 for two bands of the Sentinel 3A, OLCI sensor. These are the 443 nm and 560 nm bands. The mean and standard deviation of the change can be seen in the upper left of the figures. As can be seen and as expected, there is a negligible change to L_w1 in these wavelengths.

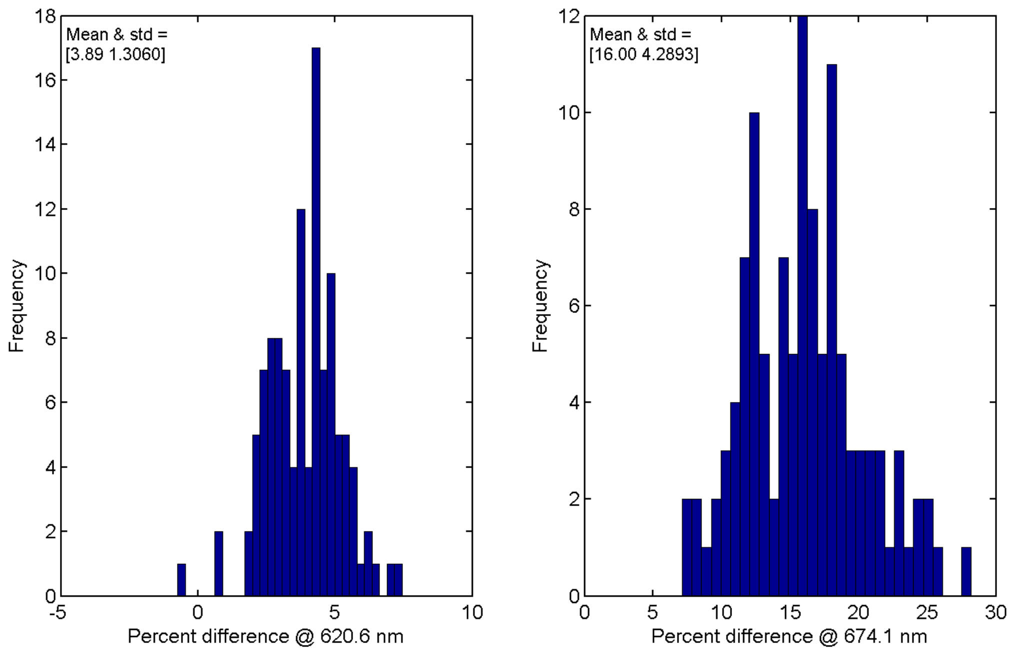

Figure 9) Similar to Fig. 8, but for the Sentinel 3A OLCI channels at 620 nm and 674 nm. As the wavelengths get longer, the effect of this change grows due to the correction for the Raman scattering and Chl fluorescence.

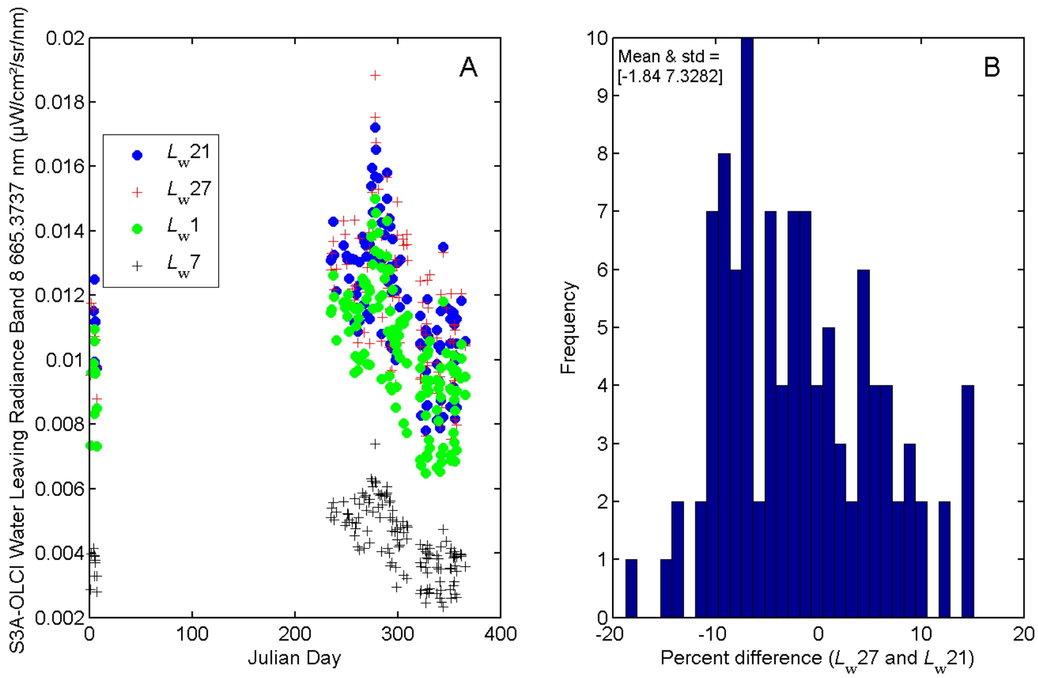

Figure 10) In panel (A) we show L_w(665 nm) resulting from the different processing procedures, as described in the text, for a recent MOBY deployment that had all three arms operational for 665 nm. L_w1 is significantly different from L_w7, L_w21 and L_w27, however the two new processing procedures (L_w21 and L_w27) agree quite closely. This is shown quantitatively in (B) where a histogram of the percent difference between L_w21 and L_w27 is presented. The bias between these products (-2%) and standard deviation (7%) are shown on the figure.